Phase-Pure Wurtzite GaAs Nanowires Grown by Self-Catalyzed Selective Area Molecular Beam Epitaxy for Advanced Laser Devices and Quantum Disks

Marvin M. Jansen [1,3,*], Pujitha Perla [1,3], Mane Kaladzhian [1,3], Nils von den Driesch [1,3], Johanna Janssen [1,3], Martina Luysberg [3,4], Mihail I. Lepsa [2,3], Detlev Grützmacher [1,2,3] and Alexander Pawlis [1,3,#]

1) Peter-Grünberg-Institute (PGI-9), Forschungszentrum Jülich GmbH, 52425 Jülich, Germany

2) Peter-Grünberg-Institute (PGI-10), Forschungszentrum Jülich GmbH, 52425 Jülich, Germany

3) JARA-Fundamentals of Future Information Technology, Jülich-Aachen Research Alliance, 52062 Aachen, Germany

4) Ernst Ruska-Centre for Microscopy and Spectroscopy with Electrons (ER-C-1), Forschungszentrum Jülich GmbH, 52425 Jülich, Germany

---

ABSTRACT: *The control of the crystal phase in self-catalyzed nanowires (NWs) is one of the central remaining open challenges in the research field of III/V semiconductor NWs. While several groups analyzed and revealed the growth dynamics, no experimental growth scheme was verified yet, which reproducibly ensures the phase-purity of binary self-catalyzed grown NWs. Here, we demonstrate the advanced control of self-catalyzed molecular beam epitaxy of GaAs nanowires with up to a grade of 100 % wurtzite (WZ) phase-purity. The evolution of the most important NW properties during the growth, namely the contract angle of the Ga droplet, the NW length and the diameter are analyzed by scanning electron microscopy and transmission electron microscopy. Based on these results, we developed a comprehensive NW growth model calculating the time-dependent evolution of the Ga droplet contact angle. Using this model, the Ga flux was dynamically modified during the growth to control and stabilize the contact angle in a certain range favoring the growth of phase-pure GaAs NWs. Although focusing on the self-catalyzed growth of WZ GaAs NWs, our model is also applicable to achieve phase-pure zinc blende (ZB) NWs and can be easily generalized to other III/V compounds. The self-catalyzed growth of such NWs may pave the way for substantial improvement of GaAs NW laser devices, the controlled growth of WZ/ZB quantum disks and novel heterostructured core/multi-shell NW systems with pristine crystalline order.*

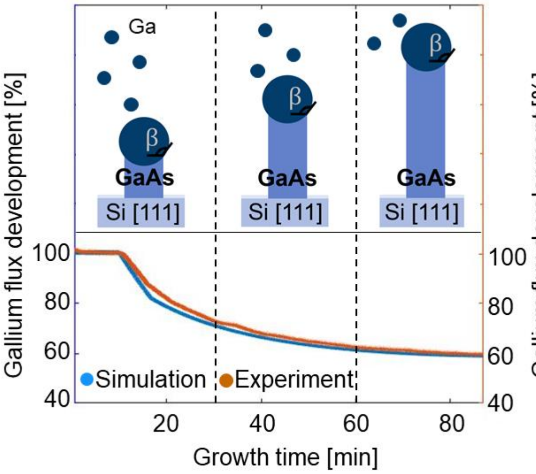

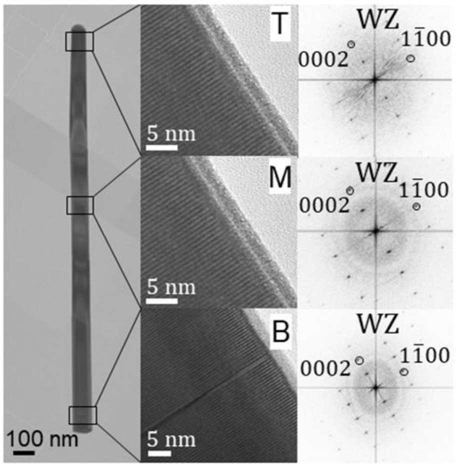

KEYWORDS: *Nanowire, vapor-liquid-solid, selective area growth, molecular-beam epitaxy, droplet contact angle, phase-pure, growth model*

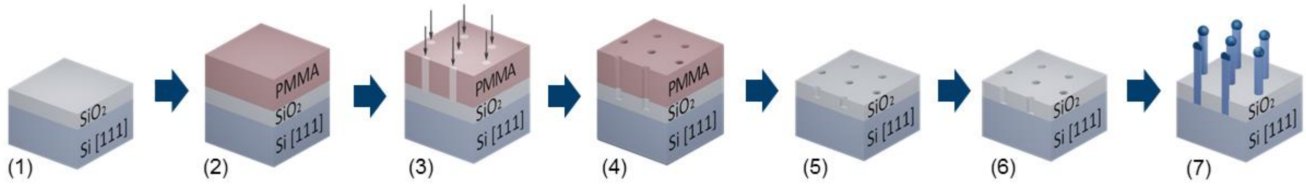

Figure 1. Substrate preparation for selective growth of self-catalyzed GaAs NW arrays. The preparation process can be divided into seven steps: (1) The growth of 20 nm thick thermal SiO_2. (2) Spin coating of PMMA. (3) Electron beam lithography of the hole array into the PMMA layer and subsequent development. (4) Pattern transfer into the SiO_2 by reactive ion etching. (5) Resist removal and wet chemical cleaning. (6) Wet chemical etching by 1% HF. (7) NW growth inside the hole arrays.

Self-catalyzed III/V semiconductor nanowires (NWs) grown by molecular beam epitaxy (MBE) provide enormous potential for miniaturized electronic and optoelectronic devices. Typical applications are advanced laser emitters[1], quantum disks[2] and single photon sources.[1,3] A main research goal in recent years was the integration of III/V NWs in silicon complementary-metal-oxide-semiconductor (CMOS) platforms. Most prominently, GaAs NWs were grown vertically via the selective area epitaxy (SAE) on (111) silicon (Si) substrates covered with silicon oxide (SiO_2). Using this method highly ordered NW arrays were fabricated with precise control of the NW length, diameter and pitch.[4–6] The growth of these NWs is based on the vapour-liquid-solid (VLS) mechanism, where the atoms nucleate at the interface between the liquid catalyst droplet and the solid NW rod. Depending on the catalyst contact angle, the NWs can crystallize in zinc blende (ZB) or wurtzite (WZ) phase, which exhibit different mechanical, [7,8] electrical[8,9] and optical properties.[10–13] The formation of either WZ or ZB crystal phase segments has been assigned to the start of the nucleation at the triple phase line (TPL) or, alternatively, inside the dropet at the liquid solid interface, respecively.[14–18]

GaAs NWs can be grown self-catalyzed with Ga or with a forgein catalyst, such as Au. For the latter, phase-pure growth of GaAs and other III/V compound NWs (*e.g.,* GaP[19]) has been successfully demonstrated and the corresponding growth dynamics are well understood.[20–22] However, the foreign catalyst element can introduce severe contaminations, which degrade the performance of specific modern applications such as single photon sources,[23] low-threshold NW lasers[24] and a wide range of heterostructured NWs with pristine crystalline order such as quantum dots,[25] hybrid core/shell systems[26] and supperlattices.[27] In contrast to the foreign catalyst based NWs, the demonstration of controlled growth of (nearly) phase-pure binary self-catalyzed III/V NWs is still an open task with many unsolved challenges, whereas the growth of Ga(As,Sb) NWs was successfully demonstrated.[28] To some extent this is a consequence of the deficit of a comprehensive theoretical model, which precisely describes the growth dynamics via evolution of the contact angle of the catalyst droplet (*i.e.,* Ga in GaAs NWs). Experimentally, the controlled formation of phase-pure ZB NWs was recently demonstrated,[29] but it also revealed the extensive formation of twin plane boundaries, wich are common for NWs in this crystal phase. To circumvent the occurrence of twin planes, defect-free A-polar ZB NWs were successfully demonstrated by Zamani *et al.*.[30] However, due to the tilted orientation of those NWs the integration in CMOS platforms is challenging on (111)-Si substrates. We believe that the growth of self-catalyzed phase-pure WZ NWs is the best approach to prohibit the formation of twin plane boundaries. Although the latter has not yet been demonstrated, the controlled implementation of small phase-pure WZ segments in different self-catalyzed ZB-mediated III/V NWs was intensively studied by Rieger *et al.*[31,32] They demonstrated the controlled inclusion of WZ segments in GaAs NWs by repeatedly consuming and refilling the Ga droplet during the growth process. The WZ segments are enclosed by highly polytype sections (WZ and ZB crystal phase in close proximity) which result from numerous transitions of the Ga droplet contact angle between high (~130°) and low (~90°) values. Recently, Panciera *et al.*[33] investigated the phase selection with *in-situ* transmission electron microscopy (TEM) measurements and identified the Ga droplet contact angle as the sole parameter to control the crystal phase. They also concluded that the WZ crystal phase is stabilized for contact angles ranging between 100° - 125°. The occurence of a phase transition close to the contact angle of ~125° was independently confirmed by Dursap *et al.*[34]. They applied *in-situ* reflection high energy electron diffraction (RHEED) to characterize the ZB-WZ transition during the growth of self-catalyzed GaAs NWs. The above mentioned studies mutually indicate that precise adjustment and *in-situ* stabilization of the contact angle of the catalyst droplet are the key parameters to achieve III/V phase-pure NWs via self-catalyzed MBE growth.

In this report, we study the SAE of GaAs NWs and provide a comprehensive model that describes the dynamics for self-catalyzed MBE growth of GaAs NWs on pre-patterned (PP) substrates. In our model we focus on the evolution of the contact angle during the growth of the NWs. The model is refined based on experimental studies of the main NW morphological properties (*i.e.,* droplet contact angle, NW length and diameter) at several intermediate growth stages. Finally, we utilize our advanced model to estimate a time-dependent Ga flux, (providing stabilization of the contact angle during growth), in order to

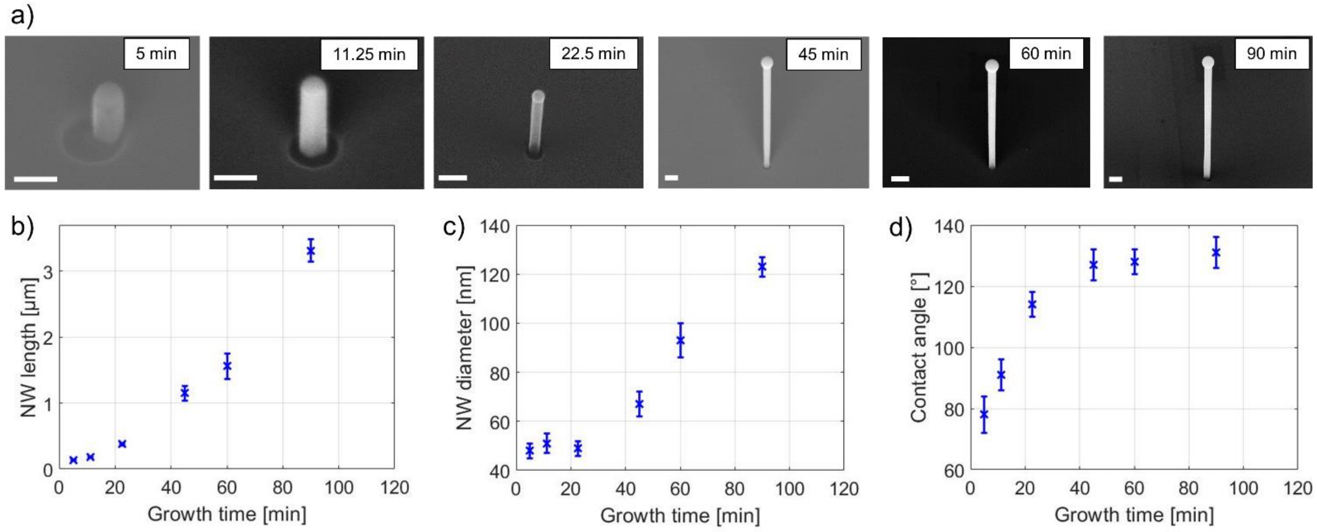

Figure 2. a) SEM images of exemplary as-grown NWs in config. A at the end of each of the growth experiments. White scale bars are 200 nm. The time-evolutions of NW length and diameter are presented in b) and c) and d) represents the time-evolution of the Ga droplet contact angle.

achieve up to 100 % phase-pure WZ (or alternatively, ZB) GaAs NWs. Our sophisticated growth model as well as the experimental verification presented in this manuscript pave the way towards a new level of advanced control over the phase-pure NW growth for innovative applications in electronics and optics such as GaAs NW laser devices and WZ/ZB quantum disks

Experimental details

The GaAs NWs were grown by MBE via the self-catalyzed VLS method on PP and n-doped (111)-Si substrates. Prior to the growth, the (111)-Si substrates are covered with a 20 nm thick thermally grown SiO_2 layer. This is subsequently patterned via electron-beam lithography and reactive ion etching to generate a set of hole arrays with different diameters d=40 – 80 nm and pitches p=0.5 – 4 µm. The preparation procedure can be divided into six process steps, which are depicted in Fig. 1. The (111)-Si substrates are covered by a 20 nm thick thermally grown SiO_2 layer (1) as a mask for the selective area growth. Subsequently, an approximately 220 nm thick PMMA-950K layer is spin coated (2). In step (3), the layout is transferred to the PMMA layer by electron-beam lithography. After that, the PMMA layer is developed with AR-600-55 for 70 s and the process is stopped by sample immersion in Isopropanol for 3 min. The first etching process is conducted by reactive ion etching (RIE), in which 10 – 15 nm of the SiO_2 is etched with a CHF_3 gas flow of 50 sccm and a RF bias power of 200 W (4). Afterwards, the PMMA layer is removed in Acetone and the patterned substrates are chemically cleaned using Piranha solution and oxygen plasma for 10 min each (5). Before loading the sample into the MBE system, it is wet chemically etched by diluted (1%) HF for another 60 s (6). After that, the sample is stored in the UHV loadlock of the III/V MBE system From the loadlock, the sample is transferred into the preparation chamber for bake-out 45 min at 700 °C and then into the III/V-MBE chamber. Prior to the NW growth the sample is heated to a substrate temperature of 620°C, which is measured by a thermocouple element (temperature calibrated with a pyrometer), and exposed for 10 min to a Ga flux that corresponds to a growth rate of about 0.1 µm/h (determined as the growth rate of a planar (100)-GaAs layer). This procedure is the Ga pre-deposition step. The NW growth is initiated by supplying an additional As_4 flux with a beam equivalent pressure (BEP) of about $5 \cdot 10^{-6}$ mbar (7), which defines a V/III BEP ratio of about 31. After the NW growth process, all cell shutters and the substrate shutter are closed immediately to minimize the post-growth during the sample cooldown and to preserve the Ga droplet contact angle. Finally, the sample is cooled down to 230 °C within 10 min. Using these parameters, a vertical NW yield of nearly 70 % was achieved. The latter was determined from the number of grown vertical NWs divided by the number of holes in the array. Considering all samples, for which the same conditions except the growth time were applied, a high grade of reproducibility of the NW yield is observed. We attribute this to our thoroughly fabrication of contamination-free PP substrates from the same preparation batch. In order to determine the stability of our fabricated PP substrates over the whole growth period, we investigated the hole diameters at three different growth stages: a) directly after preparation, b) after the Ga pre-deposition step and c) after NW growth. For all three stages we did not observe a significant variation of the hole diameters.

The Ga droplet contact angle measurements were calibrated by comparing secondary electron microscopy (SEM) images of NWs laying on TEM grids (90°) to those taken directly under tilted-view (40°). The NW diameter was always measured in the top region of the NW. A more precise overview of the resulting NW arrays is presented in the supporting information (S1).

All NW samples were characterized by SEM and the crystal structure of exemplary NWs was examined by high-resolution TEM (HR-TEM). Hereby, the NWs were harvested from the substrate and then scattered onto the TEM grids.

Results and Discussion

GaAs NW growth dynamics

GaAs NWs were grown with varying time durations between 5 and 90 min, which results in different NW lengths ranging from 0.5 to 3.5 µm. For each growth run the full set of hole diameters and pitches was analyzed by SEM measurements from which the time-evolution of NW length, diameter and the Ga droplet contact angle were extracted. A number of 5 to 15 NWs were precisely investigated for all growth times and array configurations of the PP substrates. The overall results are summarized in the supporting information section S2. In the following, we focus the discussion on one configuration, config. A, with $d = 80\ nm/p = 2\ \mu m$ (*e.g.*, diameter/pitch). For this configuration we obtained the highest vertical oriented NW yield of nearly 70 %. In Fig. 2a, exemplary SEM images of the GaAs NWs are depicted. The corresponding time-dependent evolution of NW length, diameter and contact angle are displayed in Figs. 2b-d. The error bars result from variations between the large number of investigated NW in each growth run and comprise the interval of $\pm\ \sigma$ standard deviation from the mean average value.

For config. A, the NW length increases superlinear as a function of the growth time over the entire growth period. This is also evident in the datasets of all investigated configurations (see also figures in S2). Generally, the superlinear growth is composed of two linear regimes, one corresponds to the first 20 - 30 min, while the other is observed between 30 - 90 min of growth, respectively. We attribute this double-stage NW length evolution to the interplay of competing main contribution pathways for Ga atoms feeding the catalyst droplet.[35] Once the NW length exceeds the diffusion length of Ga on the side facets, the amount of Ga diffusing from the SiO_2 surface over the side facets to the droplet is vanishing. Simultaneously, the contribution from direct impingement of Ga onto the NW side facets and subsequent diffusion to the droplet is enhanced, because the area of the side facets scales with the increasing length of the NW. At this stage, the main contribution of Ga feeding the droplet is represented by the area of the NW side facets and the surface of the droplet which scales with an increasing contact angle. The diffusion from the SiO_2 is negligible due to the low sticking coefficient of As_4.[18]

The time-dependence of the NW diameter is shown in Fig 1c. When considering all investigated configurations, we generally observe a linear dependence of NW diameter and length over the whole growth time (see also S2 in the supporting information). However, for the specific configuration A, within the first 20 min, a nearly constant NW diameter is observed, while afterwards a linear dependence is extracted.

It is straightforward that the "initial diameter" (in our experiments measured after 5 min of growth) is related to the hole diameter. The effect is most prominent within the first 20-30 min of NW growth: For config. A (hole diameter of 80 nm and pitch of 2 µm), we measured an initial NW diameter of about $d_{D80,P2} = {\sim}45\ nm$. For the same pitch, but different hole diameters, we observed a decrease to $d_{D60,P2} = {\sim}40\ nm$ for NWs grown in 60 nm holes and a further reduced one of about $d_{D40,P2} = {\sim}30\ nm$, respectively, for 40 nm holes (not shown here, see section S2 in the supporting information). The observed correlation between hole diameter and initial diameter of the NWs indicates that the start volume of the Ga droplet is determined by the hole geometry. The latter has negligible influence on NW tapering (*i.e.,* the variation of the diameter between bottom and top part of the NW), but substantially affects the initial growth dynamics presented in the theoretical section.

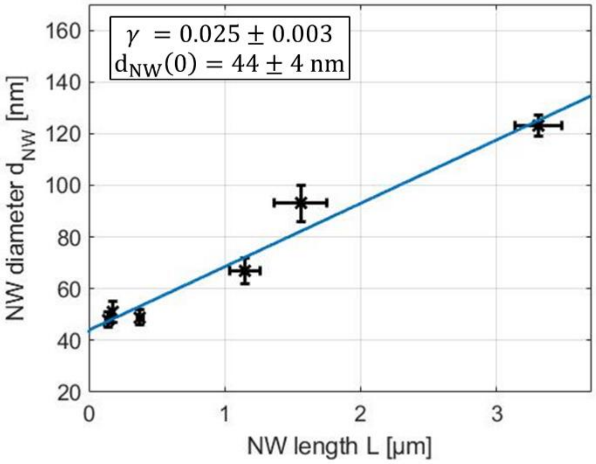

Figure 3. NW diameter d_{NW} as the function of the NW length L. The anisotropy factor and the initial NW diameter are displayed together with the corresponding standard deviations.

Figure 2d shows the time-dependent evolution of the contact angle of NWs grown in config. A. We extracted a contact angle of about 80 - 90° after 5 min of NW growth and then it rapidly increases to $\sim 125 - 130\ °$ for growth times exceeding 40 min (*i.e.,* $\sim 1\ \mu m$ NW length). This increase coincides with the quick change of the axial growth rate within the first 20 – 30 min. After that time, we observe a stabilization of the Ga droplet contact angle yielding only small fluctuations of $\pm 5°$. This experimental fact was measured for all investigated samples independently from the pitch and diameter configuration (see S3). We assume that the strong dynamic change of the contact angle at the beginning is likely responsible for the substantial increase of the axial growth rate of the NWs over the initial 20 - 30 min (see also Fig. 2b). The stabilization of the contact angle was confirmed in multiple studies on GaAs NWs with lengths exceeding $\sim 1\ \mu m$,[31,34–36] where the properties of the droplet are mainly affected by the diffusion length of Ga adatoms on the side facets of the NWs and the direct impingement on the droplet surface.

Apart from stabilization of the contact angle at longer growth times, we observed a substantial variation of the contact angles between the different configurations shortly after growth start (see S2).

Moreover, we investigated the relation between radial and axial growth rate in our samples for each pitch/diameter configuration. Figure 3 shows the NW diameter (d_{NW}) as a function of NW length (L) for config. A (dots). We found a linear dependence (full curves) where the intersection with the y-axis represents the initial diameter $d_{NW}(0) = 2r_{NW}(0)$ and the slope defines an “anisotropy factor” $\gamma = dd_{NW}/dL$ of the NW. The substantial anisotropy of axial and radial NW growth rate is a typical feature in the VLS growth regime as reported in Refs. 36,37. We observed only small variations of the anisotropy factors for different configurations (see S2). This indicates a growth dynamic that is in first order independent from the pitches and the hole diameters in our PP substrates. The anisotropy factor γ and the initial diameter $d_{NW}(0)$ represent the only two experimental parameters that are necessarily entering the diffusion model described in the following section.

Theoretical description of the kinetic growth model

To date the growth dynamics of self-catalyzed III/V NWs was described by several groups. [14, 36,38–42] Fontcuberta i Morral *et al.*[43] and Colombo *et al.*[42] pioneered the diffusion-induced VLS growth of self-catalyzed GaAs NWs on GaAs (111)B substrates covered with thin SiO_2. Dubrovskii *et al.*[14,41] and Krogstrup *et al.*[38,39] further analyzed theoretically the structural phase control of self-catalyzed GaAs NWs. The growth of WZ and ZB phases in self-catalyzed GaAs was explained by Glas *et al.*,[15] Dubrovskii *et al.*[14] and Tersoff *et al.*[44] by the different origin of the nucleation events occurring either on the TPL or inside the droplet, respectively. The nucleation theory was further refined by Schroth *et al.*[36,40] including additional features such as nearest-neighbor interactions (shadowing effects) or a variation of the radial growth rate. Microscopically, the NW growth via the VLS mechanism strongly depends on the crystal phase (ZB or WZ for GaAs NWs), the truncated facet beneath the Ga droplet and the corresponding contact angle. All these effects were recently studied in Refs. [33,45–47] using specific *in-situ* characterization techniques.

Our approach to understand the sophisticated VLS growth dynamics is founded on measurements of the time-evolution of the NW length and diameter as well as the contact angle of the Ga droplet (see previous section). Referring to recent results from Panciera *et al.*[33] and Dursap *et al.*[34] the occurrence of WZ phase is favored for contact angles between $\sim 100 - 125\,°$ while the ZB phase is obtained for contact angles <100° and >125°. According to a more generic growth study previously performed by Rieger *et al.*,[31] the time-evolution of the contact angle depends on the amount of Ga supplied to the Ga droplet during growth. In our model we consider three main contribution pathways over which the droplet is supplied with Ga and also As atoms: (1) diffusion from the SiO_2, (2) diffusion from the NW side facets and (3) direct impingement on the Ga droplet. All contributions are schematically illustrated in Fig. 4.

Based on our experimental study presented in the previous section, we assume that the fraction of Ga atoms distributed over each of the three contribution pathways varies during the first 30 - 40 min of NW growth. Shortly after the growth start, most of the Ga atoms impinging on the SiO_2 surface diffuse to the Ga droplet on top of the NW. Hence the amount of Ga atoms feeding the droplet via this pathway (1) is determined by the diffusion length $\lambda_{Ga}^{SiO_2}$ of Ga on SiO_2. For longer growth times, the number of Ga atoms diffusing from the SiO_2 and then reaching the droplet decreases with increasing NW length and vanishes once the NW length is in the same order as the diffusion length λ_{Ga}^{facets} of Ga on the side facets. At this stage the direct impingement of Ga atoms on the side facets of the NW (2) and subsequent diffusion dominates the Ga contribution to the droplet. This contribution increases with NW length and saturates to a constant value once the NW length exceeds the Ga diffusion length λ_{Ga}^{facets}. Finally, the amount of direct impingement of Ga atoms to the droplet (3) only scales with the surface area (size) of the droplet. For the As species we consider only two contributions, (2) and (3), because the sticking coefficient of As on SiO_2 is about zero and the contribution corresponding to pathway (1) vanishes.[35, 39,42]

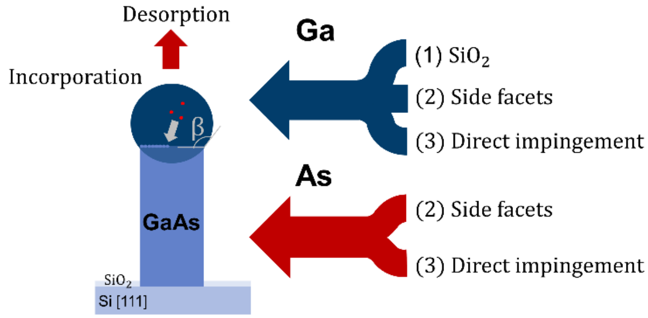

Figure 4. Schematic overview of the contribution pathways to feed Ga and As atoms to the Ga droplet. (1) Diffusion from the SiO_2, (2) diffusion from the NW side facets and (3) direct impingement on the Ga droplet.

Our model provides rate equations for both, the Ga and As fluxes to the droplet including all contributions (1-3). From these equations, the change of the length, radius and Ga droplet volume during the growth can be predicted, which ultimately allows us to control experimentally the NW crystal phase (WZ or ZB).

The number of Ga atoms impinging on the SiO_2 and diffusing to the Ga droplet in unit time is calculated by

$$N_{Ga}^{SiO_2}(L, r_{NW}) = c_{Ga}^{SiO_2} \cdot J_{\perp,Ga}^{flux} \cdot \rho_{Ga}^{facets} \cdot A_{Ga}^{SiO_2} \qquad (1)$$

where $c_{Ga}^{SiO_2}$ is the sticking coefficient of Ga atoms on SiO_2, $J_{\perp,Ga}^{flux} = J_{Ga}^{flux}\, cos(\varphi)$ is the perpendicular component of the corresponding beam flux J_{Ga}^{flux} relative to the substrate and φ is the angle between effusion cell and substrate surface. A more detailed study on the beam fluxes and the applied correction factors are presented in S3. The next term $\rho_{Ga}^{facets}(L) = e^{-L/\lambda_{Ga}^{facets}}$ represents the probability of Ga adatoms reaching the Ga droplet by diffusion from the bottom to the top of the NW. The final term $A_{Ga}^{SiO_2}(r_{NW}) = \int_{r_{NW}}^{\infty} r \cdot e^{-r/\lambda_{Ga}^{SiO_2}} dr \cdot \int_0^{2\pi} d\alpha$ defines the collection area on SiO_2, from which the Ga adatoms are transferred to the droplet. In the expression of $A_{Ga}^{SiO_2}(r_{NW})$, the term $\lambda_{Ga}^{SiO_2}$ represents the diffusion length of Ga on SiO_2 and r_{NW} is the radius of the NW.

The number of Ga or As atoms in unit time (defined by index i) impinging directly on the side facets and then diffusing to the Ga droplet is given by

$$N_i^{facets}(L, r_{NW}) = c_i^{facets} \cdot J_{\parallel,i}^{flux} A_i^{facets} \qquad (2)$$

where c_i^{facets} is the sticking coefficient of Ga or As atoms on the side facets and $J_{\parallel,i}^{flux} = J_i^{flux} sin(\varphi)$ represents the parallel component of the corresponding beam fluxes relative to the substrate. Since the NW geometry is approximated as cylindrical, the collection area on the side facets is defined as $A_i^{facets}(L, r_{NW}) = 2/3 \cdot 2\pi \cdot r_{NW} \int_0^L e^{-l/\lambda_i^{facets}} \cdot dl$, with the diffusion length of Ga or As atoms λ_i^{facets} and the NW length L. The rotation-dependent correction of $A_i^{facets}(L, r_{NW})$ is explained in more detail in S3.

Finally, the number of Ga or As atoms directly impinging on the droplet within unit time is described by

$$N_i^{direct}(\beta, r_{NW}) = J_{\perp,i}^{flux} \cdot A_\perp + A_\parallel \cdot J_{\parallel,i}^{flux}. \qquad (3)$$

For each component, the relevant surface has been considered by the area $A_\perp(r_{NW})$ and $A_\parallel(\beta, r_{NW})$, respectively. (For more details see the supplementary information S3). The variable β represents the contact angle of the Ga droplet. Note, that in contrast to other works, we neglect the effect of As re-emission as the hole density of the PP substrates is much smaller than for example in Ref. 48.

The volume $V(t)$ of the Ga droplet changes in the time interval Δt as

$$V(t + \Delta t) = V(t) + V_{Ga} \cdot [N_{Ga}^{total} - N_{Ga}^{incorp}]\Delta t \qquad (4)$$

in which Δt, the integration time in our simulation is set to 1 s. V_{Ga} is the volume of a Ga atom and

$N_{Ga}^{total} = N_{Ga}^{SiO_2} + N_{Ga}^{facets} + N_{Ga}^{direct}$ is the sum of all three contributions. We assume that the solubility of As in liquid Ga is negligible, *i.e.* each incoming As atom will take one Ga atom from the droplet to form GaAs at the interface between droplet and NW, such as $N_{Ga}^{incorp} = N_{As}^{total} = N_{As}^{facets} + N_{As}^{direct}$.

To start the simulation, we need to define the initial droplet volume, at t=0, which is calculated using equation 5,

$$V_{droplet}(t) = \frac{\pi \cdot (r_{NW}(t))^3}{3} \cdot (1 - cos\beta(t))^2 \cdot \frac{2 + cos\beta(t)}{sin^3\beta(t)} \qquad (5)$$

with the initial NW radius $r_{NW}(t = 0)$ and contact angle $\beta(t = 0)$.

The change of the NW length L(t) in the time interval Δt can be written as

$$L(t + \Delta t) = L(t) + \frac{\Omega_{GaAs}}{\pi \cdot r_{NW}{}^2} \cdot N_{Ga}^{incorp}\Delta t, \qquad (6)$$

where Ω_{GaAs} is the volume of one pair Ga-As in solid GaAs.

Finally, the change of the NW radius $r_{NW}(t)$ can be obtained

$$r(t + \Delta t) = r(t) + \frac{\gamma}{2} \cdot \frac{\Omega_{GaAs}}{\pi \cdot r_{NW}{}^2} \cdot N_{Ga}^{incorp}\Delta t, \qquad (7)$$

using the anisotropy factor $\gamma/2 = dr_{NW}/dL$ introduced in previous section. By extracting the anisotropy factor γ and the initial NW diameter $r_{NW}(0)$ from the experiments presented in Fig.2, we reduce the free parameter space of our model only to specific material constants and the initial contact angle β(0).

The full set of material parameters used for the calculation is summarized in Tab.1. The literature values indicate a wide spread of each parameter. Note, that especially the diffusion length of Ga on SiO_2 varies by about 2 orders of magnitude. In accordance with our model this diffusion length determines the collection area from which the droplet is fed at early growth stages and with that, the growth dynamics of the first ~20 min. Consequently, one would expect a substantial change of the growth dynamics once the distance of adjacent NWs approaches the Ga diffusion length on SiO2 due to overlapping collection areas. However, no experimental evidence of a substantial change of the growth dynamics as a function of the pitch (varying between 0.5 – 4 µm) in our PP substrates was observed (see also figures in S2). This gives a first indication that in our case the diffusion length of Ga on SiO_2 does not exceed 250 nm (*e.g.*, half of the smallest pitch). Hereby, the diffusion length of Ga on SiO_2 is conducted from the simulation of the experimental data, which included the integration over the silicon surface area inside the holes and the SiO_2 around the holes. The influence of the silicon surface area (representing < 3% of the collection area of pathway (1)) is included in the simulation uncertainty of the diffusion length.

Apart from that we consider the other constants in Tab.1 as independent of the diameter and pitch configuration in our PP substrates. We adjusted each of the parameters in Tab.1 to a best-fit value based on the full set of experimental data (including all configs, see Fig. 1 and S2). The obtained set of simulation parameters is given in the Model column of Tab.1. The indicated deviations are extracted from the best fit of the experimental data of all configurations and cover the interval of $\pm\,\sigma$. Considering the obtained material parameters as well-defined, our complete growth model remains with only one fitting-parameter: The initial contact angle ($\beta(0)$) which is required to calculate the starting volume of the droplet $V_{droplet}(0)$ (see Eq.5).

Parameters	Literature	Model
$c_{Ga,\mathrm{facets}}$	1.0 – 3.0 [31,35,39]	1.3 ± 0.2
c_{Ga,SiO_2}	0.07 – 1.0 [31,35,39]	0.1 ± 0.01
$\lambda_{Ga,\mathrm{facets}}$	1 - 5 µm [35,37,40,42]	2.4 ± 0.4 µm
λ_{Ga,SiO_2}	0 – 1000 nm [34,39,42,49]	200 ± 20 nm
$c_{As,\mathrm{facets}}$	0 – 1.0 [35,39]	0.04 ± 0.01
c_{As,SiO_2}	0 [39,42]	0
$\lambda_{As,\mathrm{facets}}$	0 – 300 nm [39]	50 ± 10 nm
λ_{As,SiO_2}	0 [39,43]	0

Table 1. Full set and range of parameters extracted from different literature sources. The corresponding values in the Model column are obtained by fitting the experimentally observed time-evolutions of NW length, diameter and droplet contact angle (see Fig. 1 and S4) with our growth model.

Simulation results of the time-evolution of β and L for config. A are displayed as full curves in Fig. 5a and b, respectively, and the given data points represent the experimental values. The highlighted blue region covers the interval of $\pm\,\sigma$ of $\beta(0)$, $r_{NW}(0)$ and γ as well as the standard deviation of the material parameters in our model. We gained excellent accuracy of our model describing the complex dynamics for the growth of self-catalyzed GaAs NWs on PP substrates. Significant deviation between the experimental datasets and simulated results is found only within the first ten minutes of the NW growth. We attribute this to the setting of the initial contact angle $\beta(0)$ as our remaining fitting parameter. Interestingly we achieve the best-fit for $\beta(0)$ ranging from 70 - 90°. However, the exact range of $\beta(0)$ is difficult to predict as it should depend on the microscopic topology of each hole in our PP substrates.

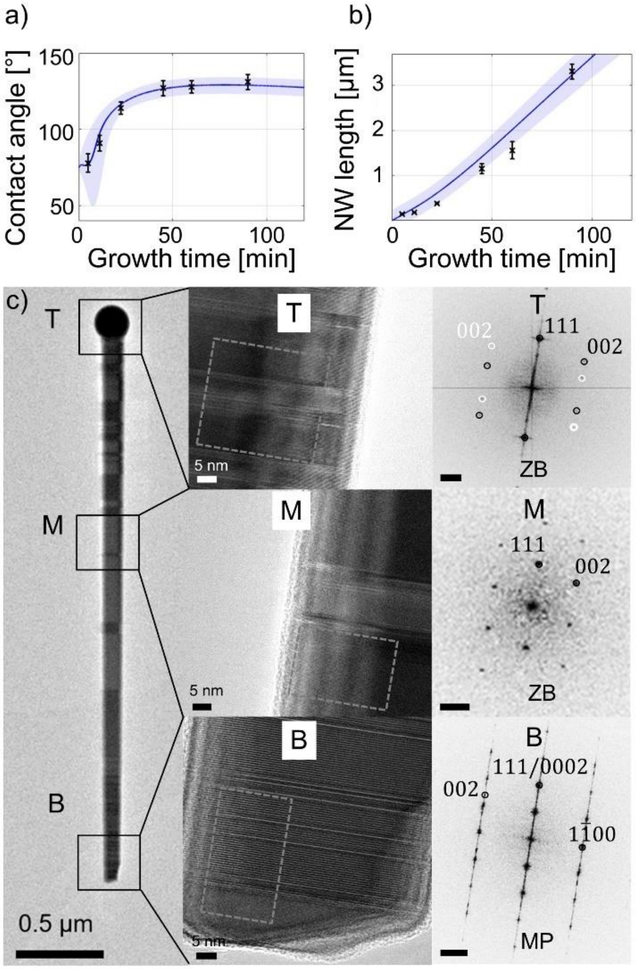

Figure 5. Time-evolution of the Ga droplet contact angle a) and corresponding NW length b) for config. A. The data points are experimental values extracted from Fig. 2. The full curves display the best-fit obtained by application of our growth model with the parameter set given in Tab.1. The light blue areas in a) and b) cover the interval of $\pm\sigma$ variation of $\beta(0)$ and $r_{NW}(0)$ as well as the error of material parameters in the model. c) HR-TEM studies (in [110] for ZB or [11$\bar{2}$0] for WZ zone axis) of a typical GaAs NW after 90 min growth time. ZB with twinning at the top (T) of the NW, large ZB segments with twinning at the middle section (M) and bottom section (B) with WZ and MP. The scale bars of the FFTs is set to 0.2 nm^{-1}.

Apart from that, we observe a rapid increase of the contact angle shortly after the growth start. We explain this by the competitive interplay of the first two contribution pathways feeding the droplet with Ga. At the initial stage of NW growth, the diffusion of Ga species from the SiO_2 to the Ga droplet plays a significant role. Here, accurate adjustment of the initial Ga flux mainly determines the dynamic start of the NW growth. After a certain length of the NWs, the amount of Ga atoms diffusing from the SiO_2 decreases substantially, while the amount of Ga atoms impinging on the side facets and subsequently diffusing to the droplet steadily increases. The latter results in an increase of the Ga droplet volume and contact angle. The contact angle stabilizes after approximately 1.0 - 1.5 µm NW length as also predicted by our model. This is a consequence of a balance between the incoming Ga and As fluxes from the side facets and direct impingement and the incorporation of both species into the growing NW. The above mentioned stabilization of the contact angle does not entail a constant droplet volume. Instead, the balance between linear increasing NW diameter (*i.e.*, a constant anisotropy factor) and the expansion of the droplet volume at the same time, result in the observed stabilization of the contact angle in our growth regime.

The correlation between the contact angle and the crystal structure of the NWs is reported by several groups mentioning a transition from ZB to WZ in the range $85^\circ - 100^\circ$ and back from WZ to ZB for angles larger than

~125°.[33,34] These findings are in agreement with the time-evolution of the contact angle in our model. The NW growth starts either with WZ crystal phase or alternatively, with ZB phase depending on the initial droplet properties. After that, the contact angle is stabilized at about 125 - 130° which is close to the boundary of the phase change from WZ back to ZB. The observed crystal phase evolution is in agreement with a comparable study on the selective area growth of self-catalyzed GaAs NWs. [50]

Figure 5c shows TEM and HR-TEM micrographs of three sections (T, M and B) localized at the top, middle and bottom region of a typical NW. The diffraction patterns of the corresponding crystal phases are shown next to the HR-TEM images. At the bottom of the nanowire (see (B) in Fig.5c) we observe alternating WZ and ZB sections with lengths ranging from 10 – 100 nm. We define this first segment of the NW as mixed phase region (MP). Here, the contact angle fluctuated close to the boundary at which both, ZB and WZ growth is possible. In the middle section (see (M) in Fig. 5c), we observe the growth of nearly phase-pure ZB segments with length up to several hundred nanometers only separated by twin planes. This is in accordance with our model proposing a rapid increase of the contact angle up to ~125° and higher within the first 40 minutes of NW growth. At the top of the NW (see (T) in Fig. 5c), the crystal phase is ZB with twin planes in close vicinity. Presumably, the contact angle fluctuated close to the ZB-WZ transition (around 125°) due to small growth instabilities. The analysis of the crystal phase confirms the good agreement between the contact angle proposed by the model and the experimentally observed one after growth of the NWs.

Phase-pure NW growth

The close connection between crystal phase of the GaAs NWs and the contact angle of the droplet is well reproduced by our growth model discussed in the previous section. Moreover, our model indicates that standard growth conditions with constant Ga and As_4 fluxes during the whole growth time lead to a strong increase of the contact angle. Since the evolution of the contact angle over time depends on the available Ga flux J_{Ga}^{flux} from the effusion cell, we can utilize our model to calculate a time-dependent $J_{Ga}^{flux}(t)$ for the specific boundary condition $d\beta/dt = 0$. Appropriate setting of this specific $J_{Ga}^{flux}(t)$ during the NW growth should lead to a fast stabilization of the contact angle to a controlled value, for which either WZ or ZB phase-pure NW growth can be ensured.

We have chosen a targeted stabilization contact angle of about ~110° to perform WZ phase-pure growth of self-catalyzed GaAs NWs. Note, that our estimated starting contact angle is substantially smaller, so that at the beginning of the growth a certain replenishment period is needed to increase the contact angle to the target value. The resulting time-evolution of the calculated Ga flux (*i.e.,* BEP of the Ga cell) is displayed in Fig. 6a (blue curve) and can be divided into three main sections: In the first ten minutes of NW growth, a constant flux is provided in order to raise β to ~110°. Within the following ~40 min a monotonically decreasing Ga flux is required to prevent further increase of β (and with that a phase transition back to ZB). Finally, an approximately constant Ga flux is applied over the remaining growth time.

We were able to accurately match calculated and experimental time-dependence of the Ga flux by regulation of the Ga cell temperature real-time during growth. The latter was achieved by introduction of multiple linear ramps of the Ga cell temperature, details are given in S2.

The Ga flux is estimated by measuring the beam equivalent pressure (BEP) as indicated by the red curve in Fig. 6a. The error analysis of the simulated curve is presented in S2 and indicates that the model errors lead to a flux variation of about ±10 %, which is comparable to the variations in the BEP measurements itself. We applied the dynamic Ga flux given in Fig.6a for the growth of three samples (*i.e.,* growth times 30 min, 60 min and 90 min) and subsequently analyzed the time-evolution of NW length and contact angle as well as the grade of phase-purity.

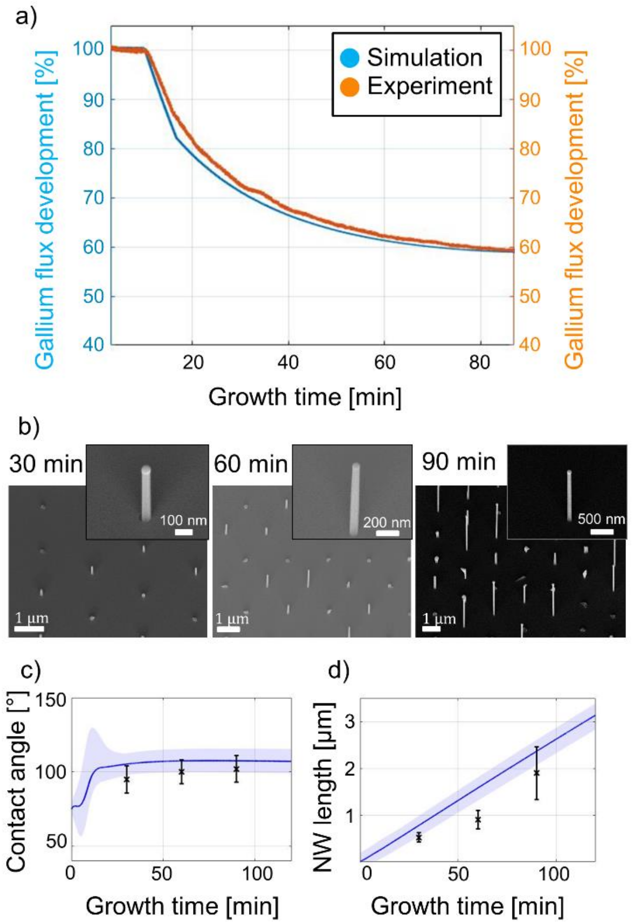

Figure 6. a) Time-evolution of the Ga flux required for WZ stabilized growth of phase-pure NWs. The blue curve was obtained from our model while the red curve corresponds to the measured Ga flux (BEP). b) SEM images of exemplary NWs after 30, 60 and 90 min growth with the dynamic Ga flux shown in a). c) Time-evolution of NW length and d) contact angle obtained from a subset of 5-10 NWs grown in config A. The black dots are the averaged measured values while the full curves are calculated with our model. The light blue areas in c) and d) cover the interval of $\pm\sigma$ variation in the model parameters.

Note, that each of the grown samples contains all combinations of pitch and diameter of the PP substrate, for which we obtained qualitatively similar results (see also S2). Figure 6b shows SEM images of exemplary NWs grown for the mentioned growth times. Frequently, we observe a slight tapering of the NWs as well as a reduction of the vertical NW yield to $\sim 20 - 30\,\%$ compared to $\sim 60 - 70\,\%$ for the previously grown NWs using a constant Ga flux. In case of inadequate starting conditions of individual NWs (*e.g.*, $r_{NW}(0)$, $\beta(0)$) the reduction of the Ga flux leads to a complete consumption of the droplet and subsequent termination of the VLS growth. These NWs (about 20 - 30 % of the holes) are not considered for the calculation of the vertical NW yield. We consider the termination as a consequence of reduction of the Ga flux, which changes the conditions for vertical and radial NW growth as well as the time-evolution of the contact angle.

For each of the three growth times, contact angle and NW length were extracted from SEM images (Fig. 6b) of 5 - 15 NWs. The average values are presented in Fig. 6c and 6d (dots) together with the calculated time-evolutions (full curves), respectively. After stabilization, Fig. 6c reveals a constant contact angle of about 110°. We observe good agreement of the time-evolution among model and experimental data, whereas the measured contact angle reveals an offset of about $\sim +7°$ to the model data. This is likely related to small variations of $\beta(0)$ and $r_{NW}(0)$, which are sensitive to the topology of individual holes in our PP substrates. Additionally, we notice a small delay between the calculated and applied $J_{Ga}^{flux}(t)$ (see Fig. 6a). However, most of the data points in Fig. 6c are comprised in the light blue area, for which we considered as before the $\pm\,\sigma$ variation of $\beta(0)$, $r_{NW}(0)$ and γ as well as the errors of the material parameters. The variation of $r_{NW}(0)$ implicates the main error in the calculation, which underlines the importance of a well-defined initial volume of the Ga droplet.

Figure 6d shows the measured (dots) and calculated (full curve) time-evolution of the NW length. For longer growth times we observe a substantial increase of the length variation among individual NWs. If the initial contact angle is smaller than 75° or the nucleation start of the NW is delayed, the reduced Ga flux will lead to premature termination of VLS growth. Considering this aspect, we extracted the NW length from those NWs only, where the VLS growth was still active (*e.g.*, indicated by the presence of the Ga droplet after growth). The model substantially overestimates the experimental values and also predicts a constant growth rate while the measured data indicate a superlinear increase of NW length. These deviations are related to our assumed initial NW radius $r_{NW}(0)$ and the anisotropy factor γ. Both values are based on the experimental datasets of NWs grown with a constant Ga flux (see Fig.3 and S2). Here, we fitted the dependence between axial and radial size of the NWs with a linear function, where the vertical intersection defines $r_{NW}(0)$ and the slope corresponds to γ, respectively. However, the observed tapering of the NWs grown with time-dependent Ga flux indicates a slight deviation from this linearity which likely induces the observed discrepancy in the NW length evolution.

The grade of phase-purity of all grown NWs was investigated by HR-TEM. Here, we focus on the crystal properties of the NWs grown for 90 min using the time-dependent Ga flux (Fig. 7) (in the following type-2 NWs), and compare them with those grown with a constant Ga flux (Fig. 5) (in the following type-1 NWs). For the other growth times, we obtained similar results, which are shortly described in S4. Figure 7a shows an exemplary HR-TEM image of a type-2 NW, which is about 1.8 µm long and exhibits 99.9% WZ phase-purity although the contact angle is substantially smaller than 90°. This can be explained by a hysteresis effect extensively discussed by Panciera *et al.*.[33] The image reveals a slight tapering of the NW (*i.e.*, bottom diameter is larger than top diameter) as previously discussed, a consequence of the dynamic Ga flux reduction.

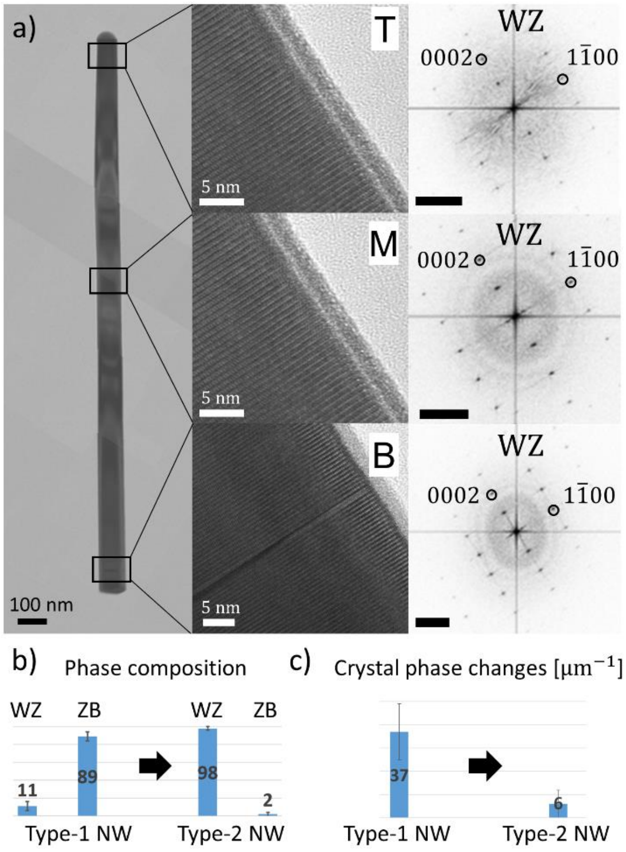

Figure 7. a) TEM image (in $[11\bar{2}0]$ zone axis) of an exemplary type-2 NW with 99.9 % phase-pure WZ crystal structure and [1120] side facets are observed. Included are inserts of HR.TEM overviews of the three main sections (T - Top, M - Middle, B- Bottom) of the NW with the respective FFT of the section. b) Grade of phase-purity estimated from HR-TEM analysis of type-1 and type-2 NWs with a typical length of about 1.8 µm (90 min growth time). c) Corresponding distribution of the quantity of phase-changes from WZ to ZB or *vice versa* per micrometer. The scale bar of the FFTs is set to 0.2 nm^{-1}.

The crystal phase was analyzed along the full NW length and high-resolution images of specific regions T, M and B (top, middle and bottom section) are presented in Fig. 7a. The bottom (B) section consist of WZ phase with two stacking faults. Overall, the NW contains five stacking faults and is otherwise 99.9% phase-pure WZ. The pristine phase-purity of this type-2 NW confirms the outstanding control over the crystal structure compared to that observed in type-1 NWs.

To confirm the impact of the dynamic Ga flux reduction proposed by our model on the grade of phase-purity of type-2 NWs, we have randomly analyzed four type-2 and four type-1 NWs grown for 90 min. We introduce two benchmark measures to quantify the observed phase distributions: (1) The grade of phase-purity is specified by the ratio between WZ and ZB segments distributed over the whole NW volume. (2) The axial phase instability is defined as the number of phase changes from WZ to ZB per micrometer of NW length. Note, this also includes stacking faults (1 ML thick ZB segments) in WZ phase-pure NWs as well as twin boundaries in phase-pure ZB NWs.

The above benchmark criteria were applied excluding the first 200 nm long segment of the as-grown type-2 NWs to account for the substantial contact angle fluctuations at the growth start. With this constraint, our overall statistics shown in Fig.7b reveals an achieved WZ crystal phase-purity of 98 ± 2 % for type-2 NWs as opposed by 89 ± 5 % ZB with 11 ± 3 % WZ crystal phase for type-1 NWs. The comparison of the axial phase instability of type-1 and type-2 NWs is presented in Fig. 7c. The latter confirms a drastic reduction in the phase instability of type-2 NWs estimated as $6 \pm 6\ \mu m^{-1}$ compared to $37 \pm 12\ \mu m^{-1}$ observed in type-1 NWs. Moreover, considering the results obtained from the analysis of overall 16 type-2 NWs including all three growth times (30 - 90 min) we found 9 revealing 99 - 100 % WZ phase, while the remaining 4 NWs yield WZ phase-purity grades of 93 - 97 %.

Additionally, we found 3 NWs revealing 99 - 100 % ZB phase. The latter are significantly longer (40 - 60 %) and thinner (40 - 60 %) compared to the WZ NWs. We assume that these NWs stem from the growth in subset C (*i.e.*, the configurations exhibiting the smallest hole diameter of 40 nm), where we observed an increased initial contact angle and a reduced NW diameter compared to those of subset A and B. More detailed analysis of a ZB NW is shown in S4.

Altogether, these benchmark results clearly emphasize the accuracy of our theoretical model describing the growth dynamics for self-catalyzed GaAs NWs grown on PP substrates. Using our comprehensive growth model, we convincingly demonstrate the advanced ability to specifically select (either WZ or ZB) and control the crystal phase of self-catalyzed GaAs NWs up to a phase-purity grade of 99 - 100 %.

Conclusions

In conclusion, we developed an elaborated kinetic model to describe the MBE of self-catalyzed GaAs NWs on prepatterned substrates. Based on a set of more than 600 individually investigated as-grown NWs we refined the relevant model parameters to accurately describe the time-evolutions of NW length and radius, as well as the contact angle of the Ga droplet when a constant Ga flux (type-1 NWs) is applied. Furthermore, we utilized our model to calculate a specific time-evolution of the Ga flux that allows to stabilize the contact angle of the Ga droplet over the whole NW growth period. We verified the excellent applicability of our model by demonstrating the growth of self-catalyzed GaAs NWs with 99 – 100 % phase-pure WZ crystal structure on PP substrates.

The developed model and the related growth strategy featuring phase-pure NWs are not limited to self-catalyzed GaAs NWs only, but can be applied to the synthesis of phase-pure NWs from various III/V material systems. Our results represent a major advance in the field of NW crystal phase engineering as the crucial basis for application of NWs in advanced laser devices, single photon sources and quantum disks.

ASSOCIATED CONTENT

Supporting Information

The Supporting Information is available free of charge via the Internet at http://pubs.acs.org

AUTHOR INFORMATION

Corresponding Authors

Marvin Marco Jansen
* E-Mail: m.jansen@fz-juelich.de
Alexander Pawlis
\# E-Mail: a.pawlis@fz-juelich.de

Authors

Pujitha Perla
Mane Kaladzhian
Nils von den Driesch
Johanna Janßen
Martina Luysberg
Mihail I Lepsa
Detlev Grützmacher
Alexander Pawlis

Author Contributions

M.M.J. and A.P. designed the experiments. M.M.J. conducted the experiments. P.P., M.I.L. and M.M.J. developed the mask design. M.M.J., A.P. and M.I.L. developed and refined the theoretical model. M.L. helped to perform and analyze the TEM images. M.K. designed the preparation graphics. M.M.J., A.P., M.I.L., N.v.d.D, M.K., J.J. and D.G. contributed to the manuscript writing. All authors have given approval to the final version of the manuscript.

ACKNOWLEDGMENT

We gratefully acknowledge the technical support by C. Krause, B. Bennemann and the cleanroom staff at the Helmholtz Nano Facility (HNF). This work was funded by the Deutsche Forschungsgemeinschaft (DFG, German Research Foundation) under Germany's Excellence Strategy – Cluster of Excellence Matter and Light for Quantum Computing (ML4Q) EXC 2004/1 – 390534769 as well as by the DFG project Nr. 337456818.

REFERENCES

1. Quan, L. N., Kang, J., Ning, C. Z. & Yang, P. Nanowires for Photonics. *Chem. Rev.* **119**, 9153–9169 (2019).
2. Corfdir, P., Van Hattem, B., Uccelli, E., Conesa-Boj, S., Lefebvre, P., Fontcuberta I Morral, A. & Phillips, R. T. Three-dimensional magneto-photoluminescence as a probe of the electronic properties of crystal-phase quantum disks in GaAs nanowires. *Nano Lett.* **13**, 5303–5310 (2013).
3. Yu, P., Li, Z., Wu, T., Wang, Y. T., Tong, X., Li, C. F., Wang, Z., Wei, S. H., Zhang, Y., Liu, H., Fu, L., Zhang, Y., Wu, J., Tan, H. H., Jagadish, C. & Wang, Z. M. Nanowire Quantum Dot Surface Engineering for High Temperature Single Photon Emission. *ACS Nano* **13**, 13492–13500 (2019).
4. Bassett, K. P., Mohseni, P. K. & Li, X. Evolution of GaAs nanowire geometry in selective area epitaxy. *Appl. Phys. Lett.* **106**, (2015).
5. Vukajlovic-Plestina, J., Kim, W., Dubrovski, V. G., Tütüncüoğlu, G., Lagier, M., Potts, H., Friedl, M. & FontcubertaMorral, A. Engineering the Size Distributions of Ordered GaAs Nanowires on Silicon. *Nano Lett.* **17**, 4101–4108 (2017).
6. Vukajlovic-Plestina, J., Kim, W., Ghisalberti, L., Varnavides, G., Tütüncuoglu, G., Potts, H., Friedl, M., Güniat, L., Carter, W. C., Dubrovskii, V. G. & Fontcuberta i Morral, A. Fundamental aspects to localize self-catalyzed III-V nanowires on silicon. *Nat. Commun.* **10**, (2019).
7. Mante, P. A., Lehmann, S., Anttu, N., Dick, K. A. & Yartsev, A. Nondestructive Complete Mechanical Characterization of Zinc Blende and Wurtzite GaAs Nanowires Using Time-Resolved Pump-Probe Spectroscopy. *Nano Lett.* **16**, 4792–4798 (2016).
8. Calahorra, Y., Kim, W., Vukajlovic-Plestina, J., Fontcuberta I Morral, A. & Kar-Narayan, S. Time-resolved open-circuit conductive atomic force microscopy for direct electromechanical characterisation. *Nanotechnology* **31**, (2020).
9. Capiod, P., Xu, T., Nys, J. P., Berthe, M., Patriarche, G., Lymperakis, L., Neugebauer, J., Caroff, P., Dunin-Borkowski, R. E., Ebert, P. & Grandidier, B. Band offsets at zincblende-wurtzite GaAs nanowire sidewall surfaces. *Appl. Phys. Lett.* **103**, (2013).
10. Swinkels, M. Y., Campo, A., Vakulov, D., Kim, W., Gagliano, L., Steinvall, S. E., Detz, H., De Luca, M., Lugstein, A., Bakkers, E., Fontcuberta i Morral, A. & Zardo, I. Measuring the Optical Absorption of Single Nanowires. *Phys. Rev. Appl.* **14**, 1 (2020).
11. Spirkoska, D., Arbiol, J., Gustafsson, a., Conesa-Boj, S., Glas, F., Zardo, I., Heigoldt, M., Gass, M. H., Bleloch, a. L., Estrade, S., Kaniber, M., Rossler, J., Peiro, F., Morante, J. R., Abstreiter, G., Samuelson, L. & Fontcuberta I Morral, a. Structural and optical properties of high quality zinc-blende/wurtzite GaAs nanowire heterostructures. *Phys. Rev. B - Condens. Matter Mater. Phys.* **80**, 1–9 (2009).
12. Ahtapodov, L., Todorovic, J., Olk, P., Mjåland, T., Slåttnes, P., Dheeraj, D. L., Van Helvoort, A. T. J., Fimland, B. O. & Weman, H. A story told by a single nanowire: Optical properties of wurtzite GaAs. *Nano Lett.* **12**, 6090–6095 (2012).
13. Vainorius, N., Lehmann, S., Gustafsson, A., Samuelson, L., Dick, K. A. & Pistol, M. E. Wurtzite GaAs Quantum Wires: One-Dimensional Subband Formation. *Nano Lett.* **16**, 2774–2780 (2016).
14. Dubrovskii, V. G., Sibirev, N. V., Harmand, J. C. & Glas, F. Growth kinetics and crystal structure of semiconductor nanowires. *Phys. Rev. B - Condens. Matter Mater. Phys.* **78**, 1–10 (2008).
15. Glas, F., Harmand, J. C. & Patriarche, G. Why does wurtzite form in nanowires of III-V zinc blende semiconductors? *Phys. Rev. Lett.* **99**, 3–6 (2007).
16. Dubrovskii, V. G., Sibirev, N. V., Cirlin, G. E., Bouravleuv, A. D., Samsonenko, Y. B., Dheeraj, D. L., Zhou, H. L., Sartel, C., Harmand, J. C., Patriarche, G. & Glas, F. Role of nonlinear effects in nanowire growth and crystal phase. *Phys. Rev. B - Condens. Matter Mater. Phys.* **80**, 1–8 (2009).
17. Spirkoska, D., Colombo, C. & Heiß, M. Growth methods and properties of high purity III-V nanowires by molecular beam epitaxy. *Adv. Solid State Phys.* **48**, 13–26 (2009).
18. Krogstrup, P., Popovitz-Biro, R., Johnson, E., Madsen, M. H., Nygård, J. & Shtrikman, H. Structural phase control in self-catalyzed growth of GaAs nanowires on silicon (111). *Nano Lett.* **10**, 4475–4482 (2010).
19. Halder, N. N., Kelrich, A., Cohen, S. & Ritter, D. Pure wurtzite GaP nanowires grown on zincblende GaP substrates by selective area vapor liquid solid epitaxy. *Nanotechnology* **28**, (2017).
20. Shtrikman, H., Popovita-Biro, R., Kretinin, A. & Heiblum, M. Stacking-faults-free zinc blende GaAs nanowires. *Nano Lett.* **9**, 215–219 (2009).
21. Shtrikman, H., Popovitz-Biro, R., Kretinin, A., Houben, L., Heiblum, M., Bukała, M., Galicka, M., Buczko, R. & Kacman, P. Method for suppression of stacking faults in wurtzite III-V nanowires. *Nano Lett.* **9**, 1506–1510 (2009).
22. Husanu, E., Ercolani, D., Gemmi, M. & Sorba, L. Growth of defect-free GaP nanowires. *Nanotechnology* **25**, (2014).
23. Harmand, J.-C., Liu, L., Patriarche, G., Tchernycheva, M., Akopian, N., Perinetti, U. & Zwiller, V. Potential of semiconductor nanowires for single photon sources. *Quantum Sens. Nanophotonic Devices VI* **7222**, 722219 (2009).
24. Mayer, B., Rudolph, D., Schnell, J., Morkötter, S., Winnerl, J., Treu, J., Müller, K., Bracher, G., Abstreiter, G., Koblmüller, G. & Finley, J. J. Lasing

from individual GaAs-AlGaAs core-shell nanowires up to room temperature. *Nat. Commun.* **4**, 1–7 (2013).

25. Akopian, N., Patriarche, G., Liu, L., Harmand, J. C. & Zwiller, V. Crystal phase quantum dots. *Nano Lett.* **10**, 1198–1201 (2010).

26. Jansen, M. M. Growth and Characterization of GaAs/ZnSe core/shell nanowires. (RWTH Aachen, 2018).

27. Heigoldt, M., Arbiol, J., Spirkoska, D., Rebled, J. M., Conesa-Boj, S., Abstreiter, G., Peiró, F., Morante, J. R. & Fontcuberta i Morral, A. Long range epitaxial growth of prismatic heterostructures on the facets of catalyst-free GaAs nanowires. *J. Mater. Chem.* **19**, 840 (2009).

28. Conesa-Boj, S., Kriegner, D., Han, X. L., Plissard, S., Wallart, X., Stangl, J., Fontcuberta I Morral, A. & Caroff, P. Gold-free ternary III-V antimonide nanowire arrays on silicon: Twin-free down to the first bilayer. *Nano Lett.* **14**, 326–332 (2014).

29. Balaghi, L., Tauchnitz, T., Hübner, R., Bischoff, L., Schneider, H., Helm, M. & Dimakis, E. Droplet-confined alternate pulsed epitaxy of GaAs nanowires on Si substrates down to CMOS-compatible temperatures. *Nano Lett.* **16**, 4032–4039 (2016).

30. Zamani, M., Tütüncüoglu, G., Martí-Sánchez, S., Francaviglia, L., Güniat, L., Ghisalberti, L., Potts, H., Friedl, M., Markov, E., Kim, W., Leran, J. B., Dubrovskii, V. G., Arbiol, J. & Fontcuberta I Morral, A. Optimizing the yield of A-polar GaAs nanowires to achieve defect-free zinc blende structure and enhanced optical functionality. *Nanoscale* **10**, 17080–17091 (2018).

31. Rieger, T., Lepsa, M. I., Schapers, T. & Grützmacher, D. Controlled wurtzite inclusions in self-catalyzed zinc blende III-V semiconductor nanowires. *J. Cryst. Growth* **378**, 506–510 (2013).

32. Rieger, T., Luysberg, M., Schaepers, T., Gruetzmacher, D. & Lepsa, M. I. Molecular beam epitaxy growth of GaAs/InAs core-shell nanowires and fabrication of InAs nanotubes. *Nano Lett.* **12**, 5559–5564 (2012).

33. Panciera, F., Baraissov, Z., Patriarche, G., Dubrovskii, V. G., Glas, F., Travers, L., Mirsaidov, U. & Harmand, J. C. Phase Selection in Self-catalyzed GaAs Nanowires. *Nano Lett.* **20**, 1669–1675 (2020).

34. Dursap, T., Vettori, M., Danescu, A., Botella, C., Regreny, P., Patriarche, G., Gendry, M. & Penuelas, J. Crystal phase engineering of self-catalyzed GaAs nanowires using a RHEED diagram. *Nanoscale Adv.* 2127–2134 (2020) doi:10.1039/d0na00273a.

35. Vettori, M., Danescu, A., Guan, X., Regreny, P., Penuelas, J. & Gendry, M. Impact of the Ga flux incidence angle on the growth kinetics of self-assisted GaAs nanowires on Si(111). *Nanoscale Adv.* (2019) doi:10.1039/c9na00443b.

36. Schroth, P., Jakob, J., Feigl, L., Mostafavi Kashani, S. M., Vogel, J., Strempfer, J., Keller, T. F., Pietsch, U. & Baumbach, T. Radial Growth of Self-Catalyzed GaAs Nanowires and the Evolution of the Liquid Ga-Droplet Studied by Time-Resolved in Situ X-ray Diffraction. *Nano Lett.* **18**, 101–108 (2018).

37. Küpers, H., Lewis, R. B., Tahraoui, A., Matalla, M., Krüger, O., Bastiman, F., Riechert, H. & Geelhaar, L. Diameter evolution of selective area grown Ga-assisted GaAs nanowires. *Nano Res.* **11**, 2885–2893 (2018).

38. Krogstrup, P., Popovitz-Biro, R., Johnson, E., Madsen, M. H., Nygård, J. & Shtrikman, H. Structural phase control in self-catalyzed growth of GaAs nanowires on silicon (111). *Nano Lett.* **10**, 4475–4482 (2010).

39. Krogstrup, P., Jørgensen, H. I., Johnson, E., Madsen, M. H., Sørensen, C. B., Fontcuberta i Morral, A., Aagesen, M., Nygård, J. & Glas, F. Advances in the theory of {III-V} nanowire growth dynamics. *J. Phys. D Appl. Phys.* **46**, 313001 (2013).

40. Schroth, P., Al Humaidi, M., Feigl, L., Jakob, J., Al Hassan, A., Davtyan, A., Küpers, H., Tahraoui, A., Geelhaar, L., Pietsch, U. & Baumbach, T. Impact of the Shadowing Effect on the Crystal Structure of Patterned Self-Catalyzed GaAs Nanowires. *Nano Lett.* **19**, 4263–4271 (2019).

41. Dubrovskii, V. G. Development of Growth Theory for Vapor-Liquid-Solid Nanowires: Contact Angle, Truncated Facets, and Crystal Phase. *Cryst. Growth Des.* **17**, 2544–2548 (2017).

42. Colombo, C., Spirkoska, D., Frimmer, M., Abstreiter, G. & Fontcuberta I Morral, a. Ga-assisted catalyst-free growth mechanism of GaAs nanowires by molecular beam epitaxy. *Phys. Rev. B - Condens. Matter Mater. Phys.* **77**, 2–6 (2008).

43. Fontcuberta I Morral, a., Colombo, C., Abstreiter, G., Arbiol, J. & Morante, J. R. Nucleation mechanism of gallium-assisted molecular beam epitaxy growth of gallium arsenide nanowires. *Appl. Phys. Lett.* **92**, (2008).

44. Tersoff, J. Stable Self-Catalyzed Growth of III-V Nanowires. *Nano Lett.* **15**, 6609–6613 (2015).

45. Jacobsson, D., Panciera, F., Tersoff, J., Reuter, M. C., Lehmann, S., Hofmann, S., Dick, K. A. & Ross, F. M. Interface dynamics and crystal phase switching in GaAs nanowires. *Nature* **531**, 317–322 (2016).

46. Panciera, F., Norton, M. M., Alam, S. B., Hofmann, S., Mølhave, K. & Ross, F. M. Controlling nanowire growth through electric field-induced deformation of the catalyst droplet. *Nat. Commun.* **7**, (2016).

47. Harmand, J. C., Patriarche, G., Glas, F., Panciera, F., Florea, I., Maurice, J. L., Travers, L. & Ollivier, Y. Atomic Step Flow on a Nanofacet. *Phys. Rev. Lett.* **121**, 166101 (2018).

48. Ramdani, M. R., Harmand, J. C., Glas, F., Patriarche, G. & Travers, L. Arsenic pathways in self-catalyzed growth of GaAs nanowires. *Cryst. Growth Des.* **13**, 91–96 (2013).

49. Heiß, M., Riedlberger, E., Spirkoska, D., Bichler, M., Abstreiter, G. & Morral, A. F. i. Growth mechanisms and optical properties of GaAs-based semiconductor microstructures by selective area epitaxy. *J. Cryst. Growth* **310**, 1049–1056 (2008).

50. Munshi, A. M., Dheeraj, D. L., Fauske, V. T., Kim, D. C., Huh, J., Reinertsen, J. F., Ahtapodov, L., Lee, K. D.,

Heidari, B., Van Helvoort, A. T. J., Fimland, B. O. & Weman, H. Position-controlled uniform GaAs nanowires on silicon using nanoimprint lithography. *Nano Lett.* **14**, 960–966 (2014).